Journal of
Intelligent Material
Systems and Structures

Original Article

Journal of Intelligent Material Systems and Structures
2018, Vol. 29(2) 265–278

DOI: 10.1177/1045389X17721037
journals.sagepub.com/home/jim
SAGE

Adaptive magnetoelastic metamaterials: A new class of magnetorheological elastomers

Ryan L Harne, Zhangxian Deng and Marcelo J Dapino

Abstract

This article reports means to significantly enhance the adaptation of static and dynamic properties using magnetorheological elastomers and demonstrates the enhancements experimentally. The tunability of traditional magnetorheological elastomers is limited by magnetic field strength and intrinsic magnetic–elastic coupling. This contrasts with recent efforts that have revealed large static and dynamic properties change in elastomeric metamaterials via exploiting internal void architectures and collapse mechanisms, although design guidelines have not been developed to adapt properties in real-time. Considering these benchmark efforts, this research integrates concepts from topologically controlled metamaterials and active magnetorheological elastomers to create and study magnetoelastic metamaterials that mutually leverage applied magnetic fields and reconfiguration of internal architectures to achieve real-time tuning of magnetoelastic metamaterial properties across orders of magnitude. Following detailed descriptions of the manufacturing procedures of magnetoelastic metamaterials, this article describes experiments that characterize the static and dynamic properties adaptation. It is found that by the new integration of internal collapse mechanisms and applied magnetic fields, magnetoelastic metamaterials can be reversibly switched from near-zero to approximately 10 kN/m in one-dimensional static stiffness and tailored to double or halve resonant frequencies for dynamic properties modulation. These ideas may fuel new research where geometry, magnetic microstructure, and structural design intersect, to advance state-of-the-art utilization of magnetorheological elastomers.

Keywords

Metamaterials, magnetorheological elastomers, adaptive properties

Introduction

Magnetorheological elastomers (MREs) have emerged as a passive–adaptive material system able to be usefully put to practice in numerous applications, with particular benefits in vibration isolation and control (Albanese and Cunefare, 2003; Lewitzke and Lee, 2001; Mayer et al., 2014; Muster and Plunkett, 1988; Porter, 2007; Yalcintas and Dai, 2004). MREs are fabricated by mixing iron particles in an elastomer matrix prior to curing. Isotropic MREs are made by curing the material in the absence of a magnetic field such that the particles have no particular alignment, while anisotropic MREs are fabricated by curing in a magnetic field such that the post-cure MRE includes aligned, iron particle chains (Bellan and Bossis, 2002; Padalka et al., 2010). Due to these particle chains, anisotropic MREs are elastically anisotropic and respond preferentially to applied fields. The anisotropy is shown to be essential to extend material tunability because there is substantially greater influence upon the anisotropic MREs from applied magnetic fields (Dorfmann and Ogden, 2003; Li et al., 2014).

These smart materials have attracted significant attention, particularly in vibration and noise control contexts (Li et al., 2013, 2014). MREs may also introduce the potential for self-powering, thus scavenging energy during non-activated operations and recycling it for later self-sufficient actuation (Chen and Liao, 2012; Choi and Wereley, 2009). Yet, despite the advantages, the property tunability is directly related to the applied field and intrinsic magnetic–elastic coupling. Large tuning requires large magnetic fields and high power, much more than can be recycled (Li et al., 2014). A

Department of Mechanical and Aerospace Engineering, The Ohio State University, Columbus, OH, USA

Corresponding author:
Ryan L Harne, Department of Mechanical and Aerospace Engineering, The Ohio State University, Columbus, OH 43210, USA.
Email: harne.3@osu.edu

new method of MRE development that requires less actuation energy and exhibits more significant magnetoelastic coupling needs to be developed.

Using conventional elastomers, recent studies on cellular, elastic metamaterials have shown that orders-of-magnitude worth of static and dynamic properties change may be achieved by leveraging internal void architectures and collapse mechanisms inherent to strategic internal material system topologies (Mullin et al., 2007; Shan et al., 2014; Shim et al., 2013). Oftentimes, the architecture constituents relatively rotate and translate as a consequence to static loading, which gives rise to large properties adaptation (Shim et al., 2013). Researchers have sought ways to leverage additional phenomena to tailor the performance of these metamaterials. For instance, Tipton et al. (2012) embedded permanent magnet cylinders into a cellular, elastic metamaterial and applied an external field to force the system into the collapsed state. It was hypothesized that this experimentally observed capability could be leveraged on many length scales as an actuation mechanism (Tipton et al., 2012). Bayat and Gordaninejad (2015a, 2015b) recently used multiphysics simulations to study the role of isotropic MRE on collapsing mechanisms for elastic wave transmission control in phononic crystals. The computational results suggested that wave transmission could be governed by the non-contact magnetic field (Bayat and Gordaninejad, 2015a, 2015b). More recently, researchers are using MREs to empower unique system-level functionality such as folding of structures for actuation purposes (Bowen et al., 2015; Crivaro et al., 2016). These studies clearly illustrate the frontier of opportunities that may be opened up by strategic use of MRE and multiphysics interactions in engineered material systems.

To summarize the developments, MRE materials are considered throughout the engineering sciences for their valuable properties change, although the greatest adaptation possible in these architectures is limited by the energy available to apply magnetic fields and extent of magnetic–elastic coupling. Also, despite the discoveries regarding cellular elastic metamaterials and recent computational studies that incorporate MRE, there is neither understanding on how anisotropic MRE may govern the properties adaptation of elastic metamaterials nor comprehensive experimental efforts that benchmark the promising tunability via the integration of magnetoelasticity and metamaterials.

Research objective and outline

The objective of this research is to investigate MREs as means for large, on-demand tuning of static and dynamic properties by integrating concepts from elastic metamaterials having internal collapse mechanisms with the established developments in MRE properties modulation. Going beyond computational studies (Bayat and Gordaninejad, 2015a, 2015b), this research articulates procedures for fabricating such magnetoelastic metamaterials (MMs) and undertakes an experimental characterization of the properties change achievable by coupling strategic internal material system topology and applied magnetic fields.

This report is organized as follows. The next section details the fabrication method for MMs. Then, experiments are reported toward elucidating the static and dynamic properties adaptation possible by concurrently leveraging collapse mechanisms and magnetic fields with MMs. A summary of conclusions and directions for future research is presented in the "Conclusion" section.

MM fabrication

As shown in Figure 1, MMs are fabricated by curing MRE materials in especially designed molds that result in a material system with internal void architectures. The MM specimen molds include standing pillars of

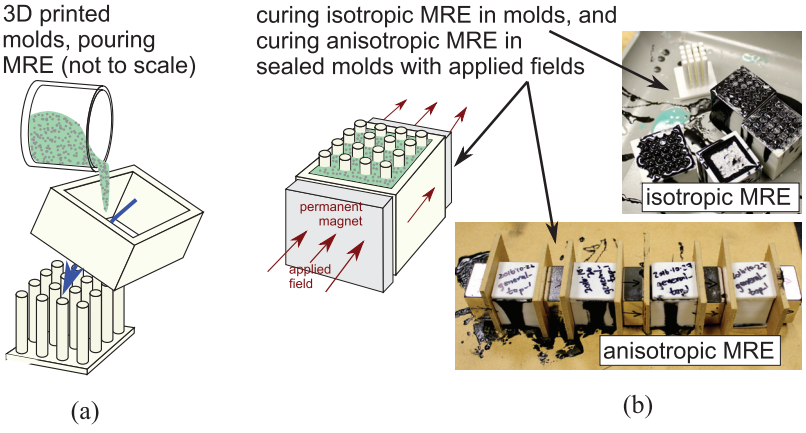

Figure 1. (a) Pouring of mixed, uncured MRE into 3D printed molds and (b) curing of MRE either without or with applied magnetic fields in order to result in isotropic or anisotropic specimens, respectively.

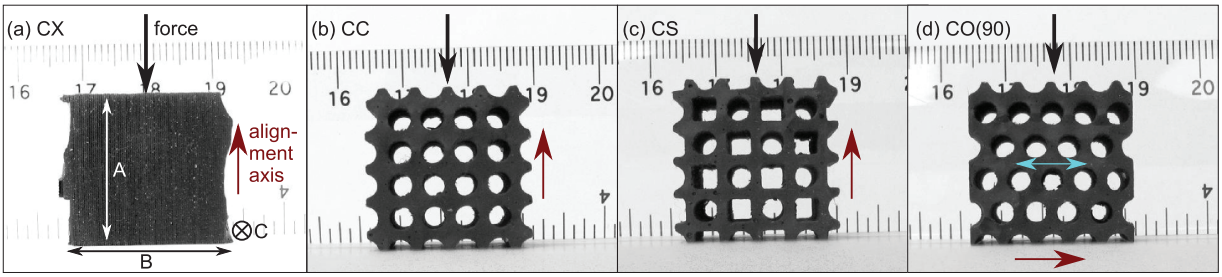

Figure 2. Samples of MRE specimens fabricated. Dimensions shown in (a), where C is the depth (into page). Arrows at the sides of specimens indicate direction of particle alignment for anisotropic (A) variants. (a) Control, CX. (b) Magnetoelastic metamaterial (MM) with CC topology. (c) MM with CS topology. (d) MM with CO topology, showing configuration corresponding to 90° angle between applied force and the elastically stiffer axis indicated by the double arrow. In other specimens, the (90) naming indicator corresponds to force application normal to the iron particle alignment.

various arrangements and forms around which the MRE cures. Anisotropic MM fabrication follows the same procedure with the addition of an external magnetic field application during the MRE curing process to generate iron particle chains within the elastomer matrix once curing is complete and field removed.

In this research, MMs are made where each specimen is approximately a cube with side length of 20.5 mm. The greatest deviation from these dimensions is about 1 [mm] across the many samples of specimens fabricated. These geometries are defined by three-dimensional (3D) printed molds made of Acrylonitrile butadiene styrene (ABS) plastic. For comparisons to the MMs, control MRE specimens are made that do not include internal architectures, so that the molds are open cubes.

The MRE is made with Mold Star 15 S (Smooth-On, Inc.), which is a two-part silicone rubber that cures at room temperature via a 1:1 mixture, and with carbonyl iron particles (BASF S-1641). The iron particles constitute about 20% of the total volume of the mixture. Once the iron particles are sufficiently mixed, the uncured MRE is poured into the molds, Figure 1(a). Once poured into the molds, the isotropic control and MM specimens are allowed to cure for 72 h before removal from the molds. For the anisotropic specimens, a 3D printed top is placed on the molds and sealed with wax. Then, on both sides of the cubes are placed rectangular magnets (Applied Magnets NB037) of slightly greater cross-section than the specimens inside the cube molds, Figure 1(b). The magnets are poled through the thickness and are oriented such that a uniform, free space magnetic field of strength approximately 1.32 T is generated within the cubic mold that separates them. These specimens are then cured for approximately 72 h before removal from the molds. Once removed from the molds, specimens are deflashed as needed.

Figure 2 surveys the specimen classes that are made in this study. Control (CX) specimens are cubes of traditional MRE without any void architectures, Figure 2(a). Specimens CC, Figure 2(b), have a circular internal void architecture in lined grids. The CS specimens, Figure 2(c), have an alternating circle and square internal architecture which induces collapse mechanisms in distinct ways and under different critical loads. Finally, the CO specimens use an internal architecture of circular voids in lines that are offset from one to another. This CO void arrangement induces elastic anisotropy due to a continuous line of MRE through one axis of the specimens, which is the horizontal axis as seen in Figure 2(d). For CX, CC, and CS specimens composed of anisotropic MRE, the anisotropic iron particle alignment axis does not preferentially couple with elastic properties since the elastic properties are ideally invariant under a rotation of 90° according to the view in Figure 2. The CO specimens composed of anisotropic MRE are cured in a way such that the alignment axis of iron particles corresponds to the axis of continuous MRE that extends through the specimen, which is shown by the double arrow in Figure 2(d).

In this study, a naming procedure is used for the classes of specimens made and experimentally examined. Either an "I" for isotropic or "A" for anisotropic begins the name, which denotes the MRE usage. Then, the specimen class is provided, such as CC. Finally, for specimens loaded in an axis that is normal (90° rotated) relative to the iron particle alignment (or anisotropic elastic axis for the CO specimens), a (90) succeeds the name. For example, I-CC means the isotropic specimen with a lined grid of circle internal void architectures, while A-CO(90) refers to the specimen composed from anisotropic MRE using the offset grid of internal circular voids. Note that I-CO(90) is the only *isotropic* specimen that has distinct properties when loaded in the axis normal to the direction of the continuous line of MRE since the CO specimen class has anisotropic elastic properties (whether or not it is composed using isotropic or anisotropic MRE).

Mechanical properties characterization

Experimental setup

Following fabrication of the various specimen classes and MRE compositions, experimental studies are

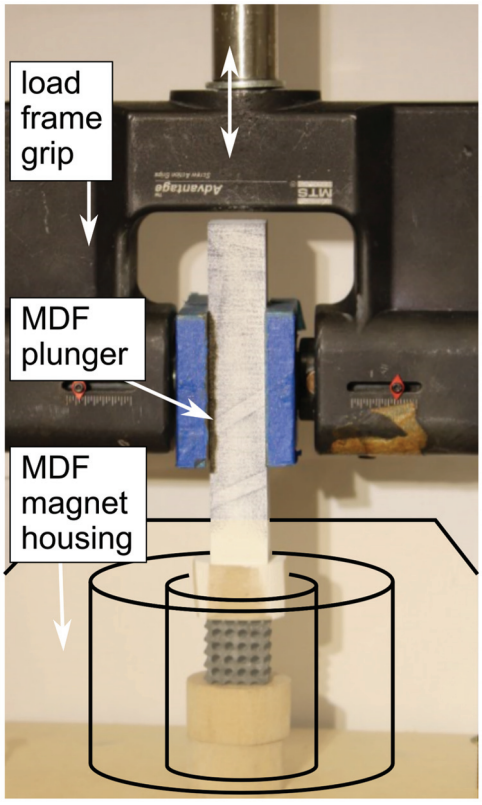

Figure 3. Load frame experimental setup indicating locations and mount methods for magnets for the applied field.

conducted to characterize the reaction load and stiffness characteristics. Figure 3 provides a photograph of the experimental setup. A load frame (TestResources 1000) with load cell (MLP-50) generates one-dimensional displacements and measures a quasi-static axial force up to 220.5 N along the output shaft direction, which is the direction shown in Figure 3 by the double arrow. A grip attaches to the end of the shaft to hold a medium-density fiberboard (MDF) plunger, which delivers a prescribed displacement to the specimens. The MDF material does not interfere with the force measurements via ferromagnetic influences related to the externally applied magnetic field. For the experiments that are conducted with an applied magnetic field, an MDF housing is inserted around the plunger on which the specimen rests and through which the load frame plunger displaces, so that the specimen is at the center of the housing and thus at a location of uniform magnetic field. The housing contains a stack of annular permanent magnets (RZ0X84; K&J Magnetics, Inc.) that provides a free space magnetic field of 3.3 T. Whereas the rectangular magnets used for fabrication are found useful for that purpose, the annular magnets used for the properties characterization studies are likewise found preferable to provide a uniform field through the specimens while concurrently providing access to deform the specimens via static and dynamic loads.

The front surface of the plunger driven by the load frame shaft is sprayed with non-reflective paint and then printed with scattered black dots. A digital image correlation (DIC) system tracks the movement of the dots and thus accurately determines the displacement of the plunger. This DIC measurement is considered to be the deformation applied to the specimens that is otherwise not visible during experiments with the applied field due to visual obstruction by the MDF housing. The load frame is operated in displacement-control mode. The maximum strain rate is 1.3%/s such that the specimens can be considered as being loaded in quasi-static state of plane strain, although negligible out-of-plane deformation also occurs that is not anticipated to greatly influence results or conclusions. The maximum compressive loads during each characterization test are selected such that the MM specimen undergoes both local collapse and uniform buckling. The strain rates and the maximum forces in this study are summarized in Tables 1 and 2 for isotropic and anisotropic specimens, respectively. Mass and dimensional information for all specimens are also given in Tables 1 and 2, where the dimensions are those labeled in Figure 2(a). All data reported from the quasi-static measurements are acquired after at least three loading and unloading cycles have been conducted. Due to the use of ferromagnetic components (MTS grip) near to the applied magnetic field, the influence of the field on the load cell force measurements is identified by conducting tests without specimens in place. Thereafter, and in all data reported herein, the magnetic force from the steel load frame grip and the permanent magnets is eliminated from the force measurements. For clarity, all measurements reported here consider compressive loads and strains; thus, strain values provided indicate the extent compressed from an undeformed configuration.

Table 1. Strain rates, maximum compressive forces, mass, and dimensions for isotropic specimens.

Specimen class	I-CX	I-CC	I-CS	I-CO	I-CO(90)
Strain rate (%/s)	1.3	0.9	0.9	1.2	0.9
Maximum force (N)	35.6	17.8	13.3	35.6	22.2
Mass (g)	13.6	9.19	7.83	9.30	9.30
A, B, C (mm)	20.0, 20.0, 20.0	21.3, 21.0, 21.0	21.0, 20.7, 20.3	21.0, 21.5, 20.0	21.5, 21.0, 20.0

Table 2. Strain rates, maximum compressive forces, mass, and dimensions for anisotropic specimens.

Specimen class	A-CX	A-CX(90)	A-CC	A-CC(90)	A-CS	A-CS(90)	A-CO	A-CO(90)
Strain rate (%/s)	1.3	1.3	0.8	0.9	0.9	0.9	0.9	1.3
Maximum force (N)	35.6	35.6	17.8	17.8	13.3	13.3	26.7	35.6
Mass (g)	12.8		8.27		7.33		8.35	
A, B, C (mm)	19.5, 20.0, 20.0	20.0, 19.5, 20.0	21.5, 21.3, 19.5	21.3, 21.5, 19.5	21.2, 21.3, 20.0	21.3, 21.2, 20.0	20.3, 20.9, 20.0	20.9, 20.3, 20.0

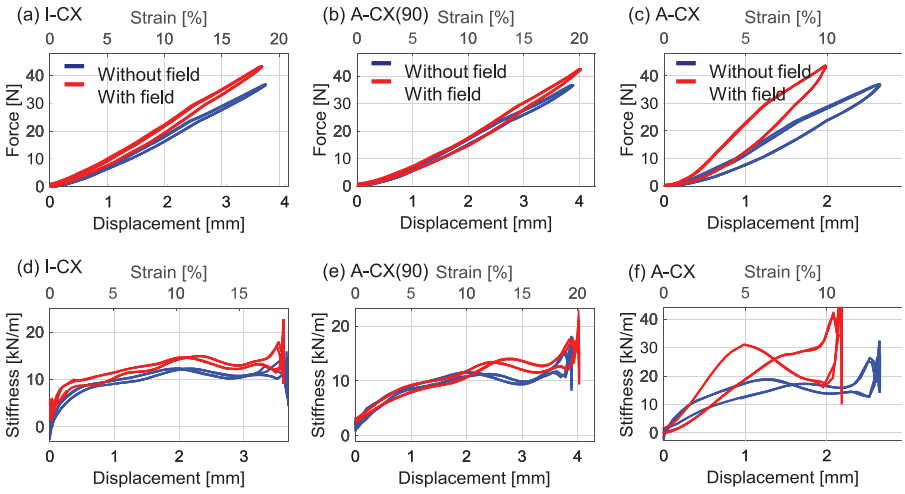

Figure 4. (a–c) present measurements of reaction force on the CX specimens due to an applied displacement; (d–f) show derived stiffnesses respectively corresponding to the measurements in (a–c).

Results and discussion

Figure 4(a) to (c) compares the force–displacement profiles for the I-/A-CX (control) specimens with and without magnetic fields. The magnetic field uniformly stiffens the control specimen, whether it is isotropic, Figure 4(a), or anisotropic, Figure 4(b) and (c). The stiffness of iron particles K_i in the MRE composition is much greater than the stiffness of the elastomer matrix K_e. With the field applied to the I-CX specimen, while the stiffness does increase, Figure 4(a) and (d), it is not a dramatic shift since the iron particles only individually rotate to more closely align with the field, Figure 5(a). On the other hand, for the A-CX(90) specimen, when the iron particles are initially aligned perpendicular to the direction of force and field application, as shown in Figure 5(b), the iron particles and elastomer matrix are connected in series and the stiffness of the elastomer matrix K_e dominates regardless of the presence of an external magnetic field. Hence, the stiffness variation due to application of the field is negligible for A-CX(90), as shown in Figure 4(e). In contrast, for the specimen A-CX that is loaded in the same axis as the iron particle alignment, as shown in Figure 5(c), the iron particles and elastomer matrix are equivalent to two springs connected in parallel between shared moving ends. In this case, the stiffness of iron particles K_e dominates. Hence, the iron particles are effectively made rigid into chains as the external magnetic field is introduced which causes a significant change in stiffness. As a result, the stiffness variation of the A-CX specimen due to applied field is the most significant, as shown in Figure 4(f) when compared to Figure 4(d) and (e).

Due to the presence of internal void architectures, the MM specimens exhibit greater mechanical properties adaptation than the CX baselines. Figure 6 shows the force–displacement measurements and derived stiffnesses of I-/A-CC specimens. This MM class exhibits a linear elastic response for strains less than approximately 10% without applied field. As the strain increases beyond this range, an internal collapse mechanism is triggered, which results in a dramatic reduction in stiffness, for example, around strain of 19% in Figure 6(d) for the I-CC. The instantaneous stiffness may be so low as to exhibit negative values. This collapse mechanism for the CC MM class, featured in Figure 7 and revealing a negative Poisson's ratio, contrasts with the traditional lateral, outward bulging of the CX specimens due to the same compressive force. For strains beyond the collapse phenomena for the CC specimens, compaction occurs and thus the

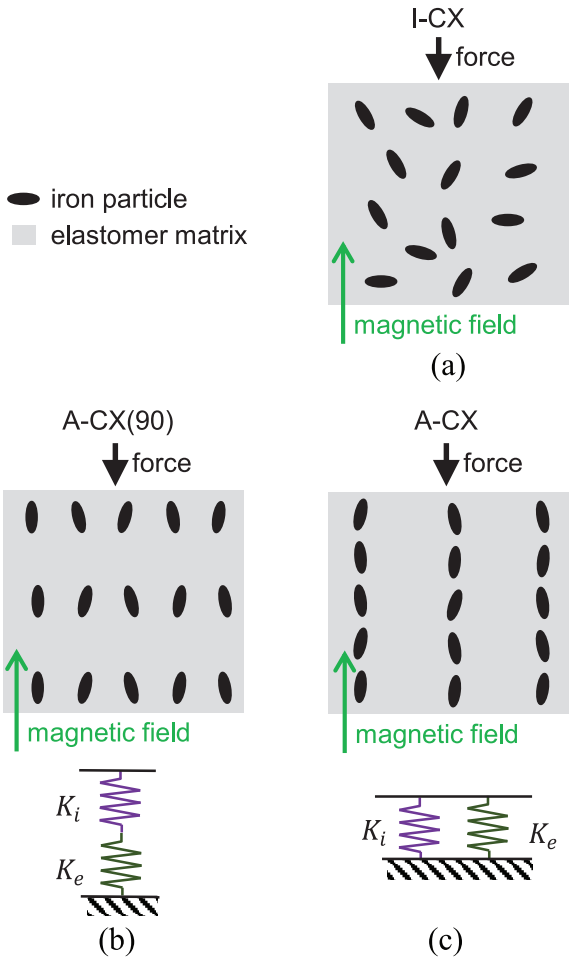

Figure 5. Iron particles' orientations under applied magnetic field for isotropic and anisotropic control specimens: (a) I-CX, (b) A-CX (90), and (c) A-CX.

load and instantaneous stiffness both increase substantially, as shown in Figure 6(a) to (c) for strains approximately 35% and greater.

Application of a magnetic field for I-CC increases the stiffness of the specimen primarily within the range of applied strains that results in the collapse effect, Figure 6(d). Thus, while for the I-CC specimen without the field, the instantaneous stiffness may be *negative*, the same specimen with field applied exhibits a *positive* stiffness. For CC specimens in general, the measurements in Figure 6(d) to (f) show that the magnetic field has far more influence on the mechanical properties than for the control CX specimens. Without the magnetic field, CC specimens deform in similar ways, whether composed from isotropic or anisotropic MRE, Figure 6(d) to (f). This indicates that the mechanical properties of the CC class are much more strongly governed by the internal void architectures than due to the underlying MRE material when the field is absent. Yet, once the magnetic field is applied, Figure 6(b) shows that the A-CC(90) undergoes the internal collapse at zero strain due to the large magnetic moment. The result is a nonlinear hardening property associated with compaction, which is why the stiffness shown in Figure 6(e) for A-CC(90) under a magnetic field uniformly increases with increase in compressive strain. Thus, as shown in Figure 6(e), turning on and off the magnetic field can vary the instantaneous stiffness from near-zero to large finite values on the order of 10 kN/m, such as around a strain of 20%–30%.

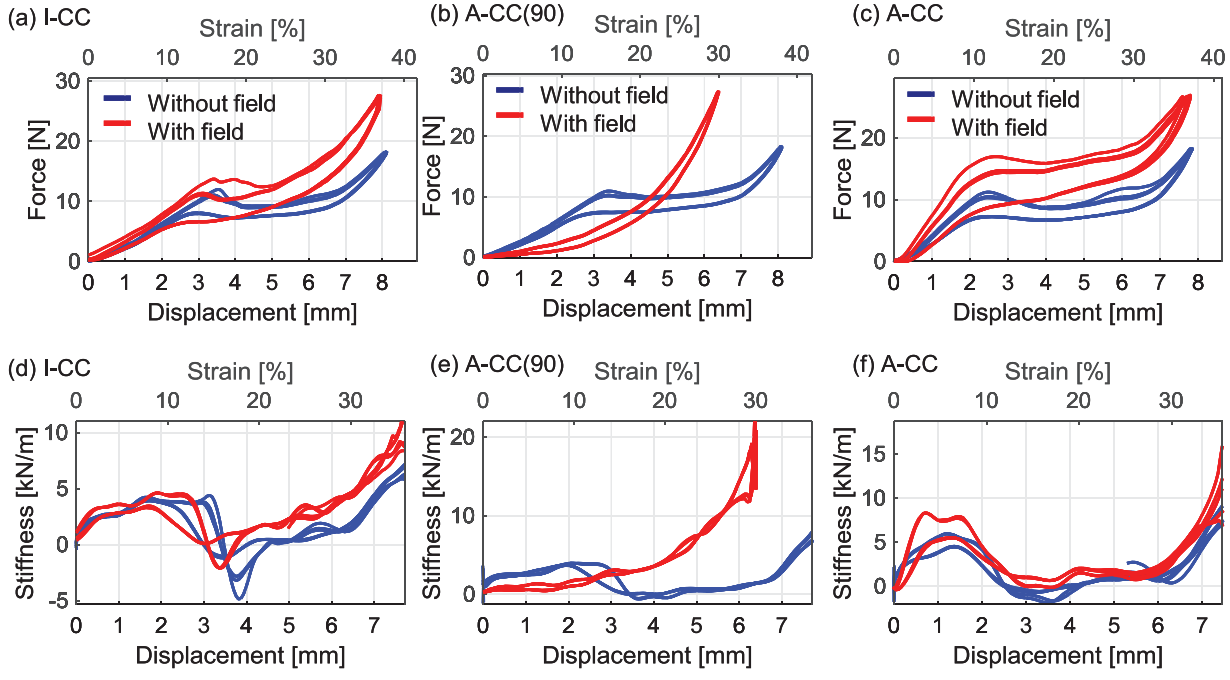

Figure 6. (a–c) present measurements of reaction force on the CC specimens due to applied displacement; (d–f) show derived stiffnesses respectively corresponding to the measurements in (a–c).

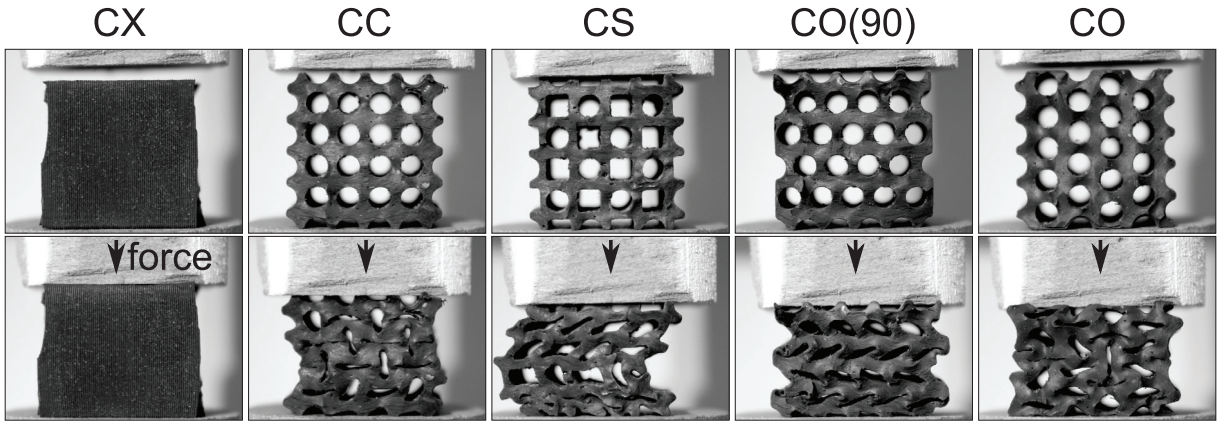

Figure 7. Deformation characteristics and distinct collapse mechanisms for specimens studied in this research. Force direction in the bottom row is indicated by the arrow.

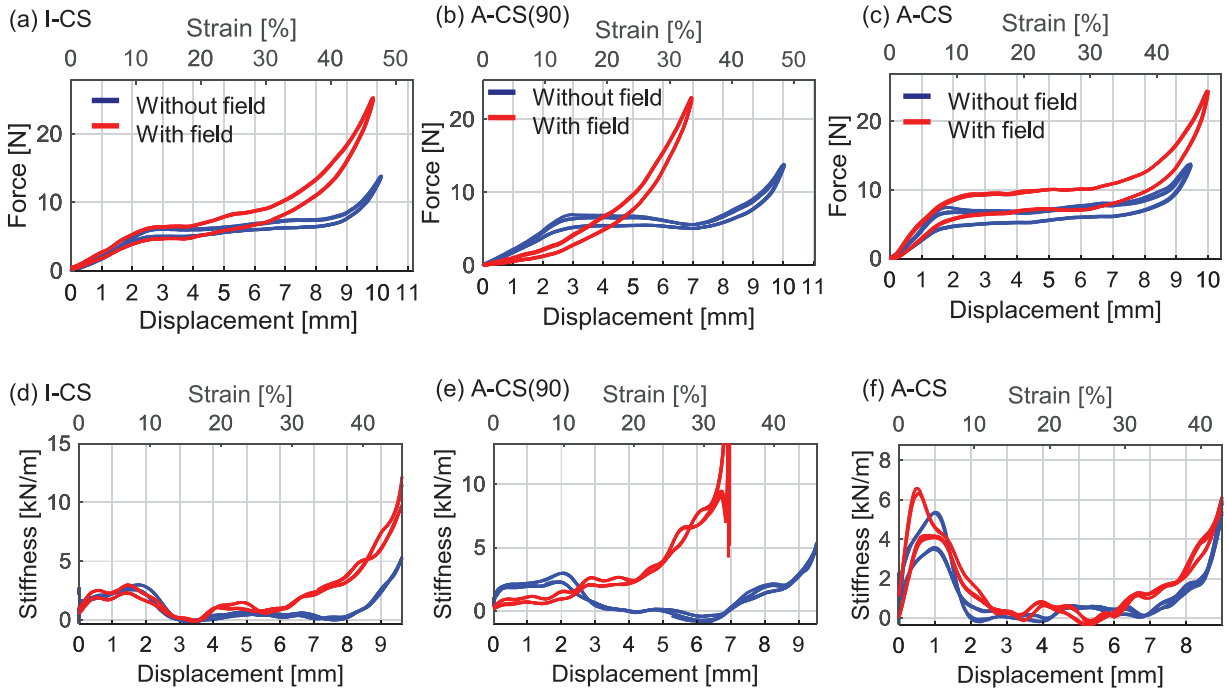

Figure 8. (a–c) present measurements of reaction force on the CS specimens due to applied displacement; (d–f) show derived stiffnesses respectively corresponding to the measurements in (a–c).

Figure 8 presents the reaction forces and derived stiffnesses for I-/A-CS MM specimens. Similar to CC specimens, a nonlinear region where the instantaneous stiffness approaches vanishingly small values occurs due to the local collapse observed from around 10%–30% strain, Figure 8(d) to (f). On the other hand, this collapse behavior is distinct, as shown in Figure 7 where it is revealed that CS specimens undergo buckling of the bulk architecture rather than a negative Poisson's ratio-type deformation observed for the CC MM specimens. Outside of the strain region of collapse, the CS MM specimens behave linearly for low strain input and exhibit increased stiffness for high strain. Application of a magnetic field increases specimen stiffness consistently. For A-CS(90), the magnetic field is also strong enough to collapse the voids and cause buckling of the bulk specimen, which results in compaction for increased strain, as shown in Figure 8(b) and (e). However, for A-CS, the external field has almost no influence on the stiffness at the local collapsing region: the stiffness is close to zero within the strain range from 10% to 30% with and without magnetic field applied, as shown in Figure 8(c) and (f). This suggests that the static properties of the A-CS MM are primarily determined by the internal collapse mechanism, regardless of the additional

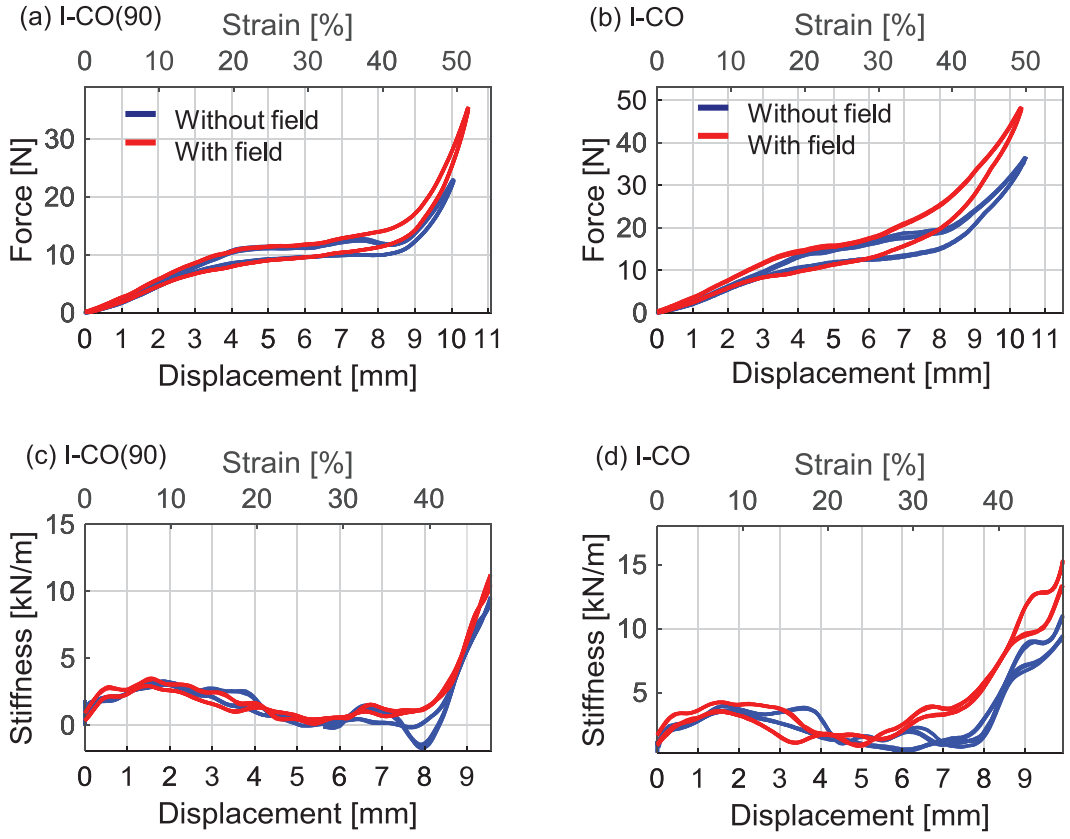

Figure 9. (a, b) present measurements of reaction force on the I-CO specimens due to applied displacement/strain; (c, d) show derived stiffnesses respectively corresponding to the measurements in (a, b).

elastic anisotropy introduced by aligned iron particle chains and despite the application of a magnetic field.

Figure 9 presents the reaction forces and corresponding stiffnesses for the I-CO MM specimens. Similar to CC and CS specimens, a nonlinear region where the instantaneous stiffness approaches zero is observed between 20% and 40% strain. The collapse mechanisms associated with these behaviors are shown in Figure 7, revealing a layer-by-layer collapse for CO(90) and an inwardly-driven collapse for CO which is similar to but not identical to the collapse for CC MMs. For these isotropic CO specimens, the magnetic field only slightly increases specimen stiffness, and primarily at higher strains, such as around 40% or greater strain, Figure 9(a) and (b). Because the application of the magnetic field only moderately changes the stiffness of the specimens when compared to the stiffness change induced by the internal reconfiguration of the specimens, it is apparent that this MM internal architecture plays the dominant role toward governing the mechanical properties.

The measurements obtained for the corresponding A-CO specimens are given in Figure 10. While the collapse behavior is likewise observed from strains 20% and 40% input strain, a much more significant influence of the applied magnetic field is found for the instantaneous stiffness throughout all of the strains considered. Notably, for the A-CO MM, application of a field around strains of 20% is one means to switch on-demand from near-zero to approximately 2 or 3 kN/m in stiffness, giving evidence of significant control of MM static properties.

Dynamic force transmissibility evaluation

Experimental setup

Force transmissibility experiments are undertaken to characterize the range of dynamic properties exhibited by the MMs through combined collapse mechanisms and applied magnetic fields.

The experimental setup for measuring the force transmissibility is shown in Figure 11(a). An electrodynamic shaker (LDS V408) is fed a slowly sweeping continuous frequency drive signal through a power amplifier (Crown XLS-1500), which then connects to a force transducer (PCB 208C01) and MDF excitation plunger, Figure 11(b). The excitation plunger and force transducer are mated with another plunger and force transducer attached to the fixed end of the experimental setup. The plungers are fabricated from MDF to eliminate magnetic force in between the permanent

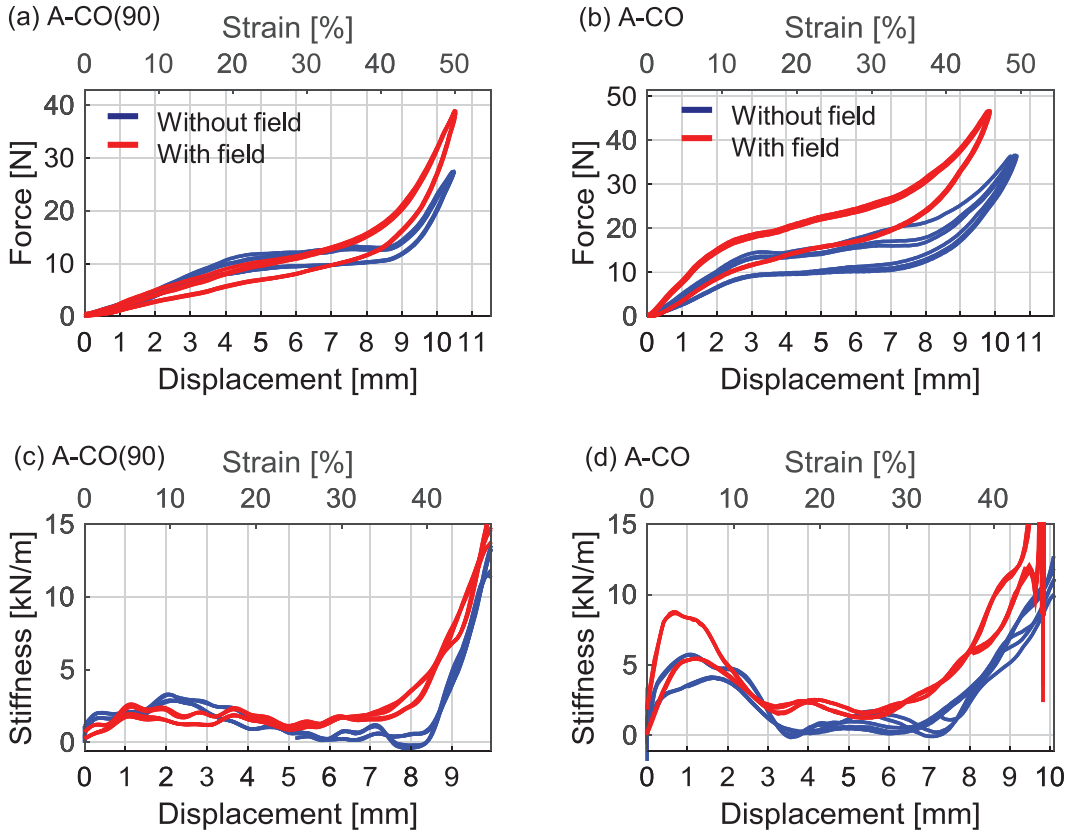

Figure 10. (a, b) present measurements of reaction force on the A-CO specimens due to applied displacement/strain; (c, d) show derived stiffnesses respectively corresponding to the measurements in (a, b).

Table 3. Pre-strain applied to isotropic specimens during dynamic characterizations with and without field.

Specimen class	I-CX	I-CC	I-CS	I-CO	I-CO(90)
Strain (%) with field	2.50, 5.00	7.04, 10.8, 17.8	4.76, 12.9, 15.7	4.65, 9.30, 13.9	4.76, 16.7, 19.0
Strain (%) without field	1.00, 5.00	6.10, 15.5, 19.2	4.76, 14.7, 18.1	5.12, 9.30, 16.3	4.76. 15.2, 16.7

magnets and the plungers. Prior to the start of a test, the specimens are placed between the two plungers and given a pre-strain ε to hold them in place. Tables 3 to 5 present the pre-strain values used for I-, A-, and A-(90) type specimens, respectively. These strain values have corresponding force transmissibility (FT) plots in Figures 12 to 14. Likewise, these are comparable to the strains reported through Figures 4, 6, 8 to 10 which will be used, in the following discussions, to correlate the pre-strains applied in dynamic tests to the various onset and occurrence of collapse mechanisms. By virtue of this specific experimental undertaking, care is taken to position and pre-strain the specimens between the two plungers so as to not induce out-of-plane deformation. When experiments are conducted with an applied magnetic field, the MDF housing and interior annular magnet set used in the mechanical properties characterization are employed, providing a free space magnetic field of 3.3 T. Thus, the field adaption of each MM specimen is considered as a binary, on/off application via the permanent magnets. While variable control of the applied magnetic field may enable an examination of the different extents to which properties adaptation is realized in the MM specimens, the following efforts provide a first account of the more straightforward and binary type of magnetic field control for properties tuning, via positioning of the permanent annular magnets.

To account for the effect of the magnets on the experimental hardware, tests are initially conducted with no specimen in place, with and without magnets. The force transmissibility transfer functions from these measurements are subtracted from the measurements taken with specimens in place.

Table 4. Pre-strain applied to anisotropic specimens during dynamic characterizations with and without field, where input and output forces are in the same axis as the anisotropic particle alignment.

Specimen class	A-CX	A-CC	A-CS	A-CO
Strain (%) with field	1.51, 4.04	6.70, 11.6, 17.7	5.71, 8.09, 10.9	2.90, 9.09, 13.0
Strain (%) without field	2.02, 6.06	5.58, 16.3, 18.6	3.33, 7.62, 12.8, 15.7	4.35, 10.6, 15.0

Table 5. Pre-strain applied to anisotropic specimens during dynamic characterizations with and without field, where input and output forces are normal to the axis of the anisotropic particle alignment.

Specimen class	A-CX(90)	A-CC(90)	A-CS(90)	A-CO(90)
Strain (%) with field	3.50, 9.00	7.51, 13.1, 17.8	3.38, 11.6, 14.5	3.35, 9.09, 16.3, 18.7
Strain (%) without field	7.50, 15.0	4.69, 14.1, 18.3	10.1, 12.1, 15.5	4.31, 11.0, 14.8, 15.8

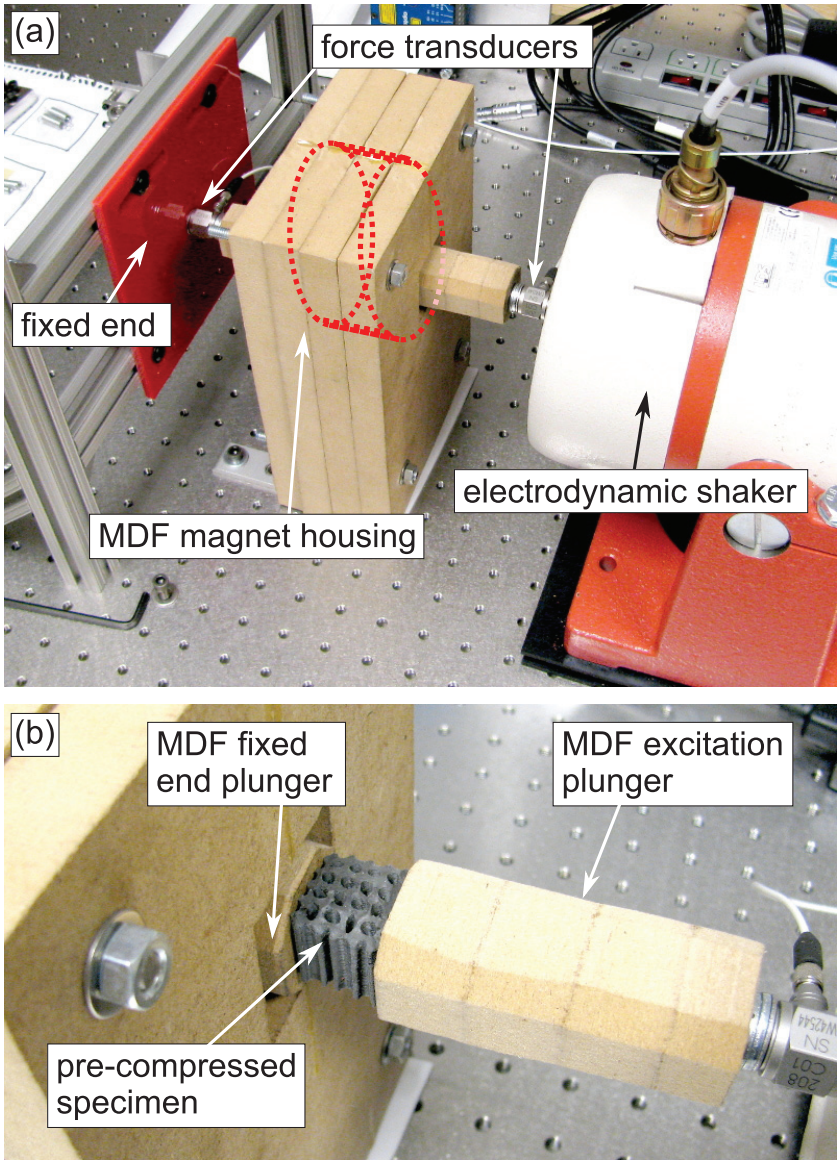

Figure 11. (a, b) Experimental setup for characterizing dynamic force transmissibility through MM specimens. (b) A close-up view of the mount and standoff method for specimens once compressed between MDF plungers.

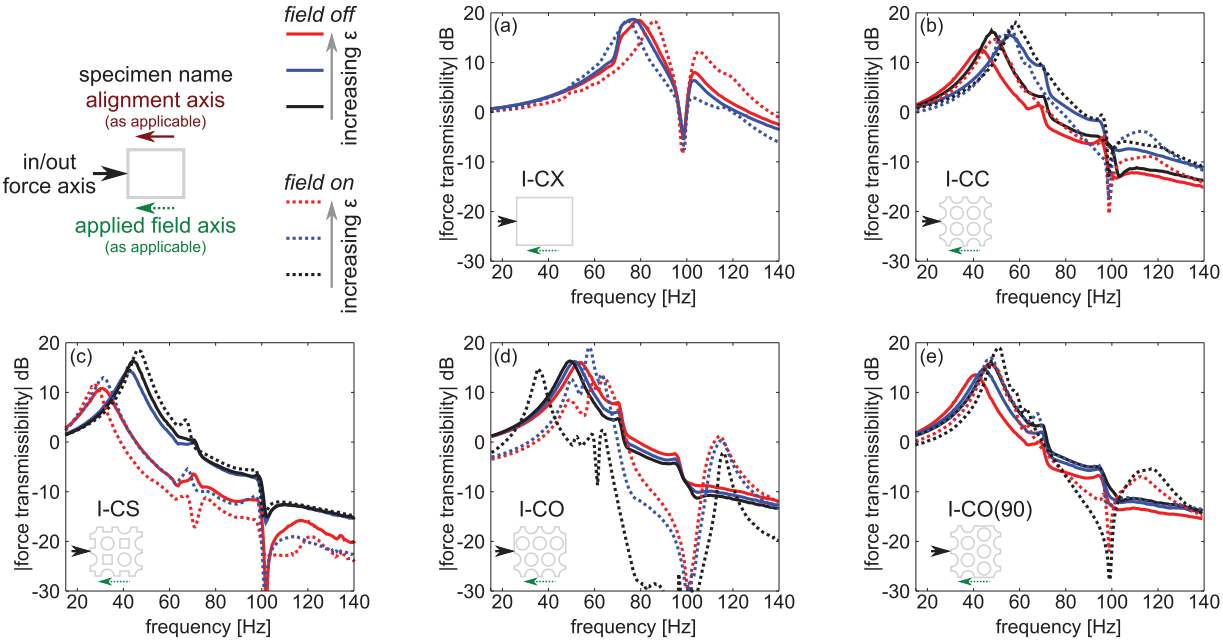

Figure 12. At top left are the inset conventions for the specimen class, and excitation, alignment, and field axes, as applicable, and legends for degrees of pre-strain ε shown in the subsequent plots. (a–e) Dynamic force transmissibility measurements for isotropic (I) specimens.

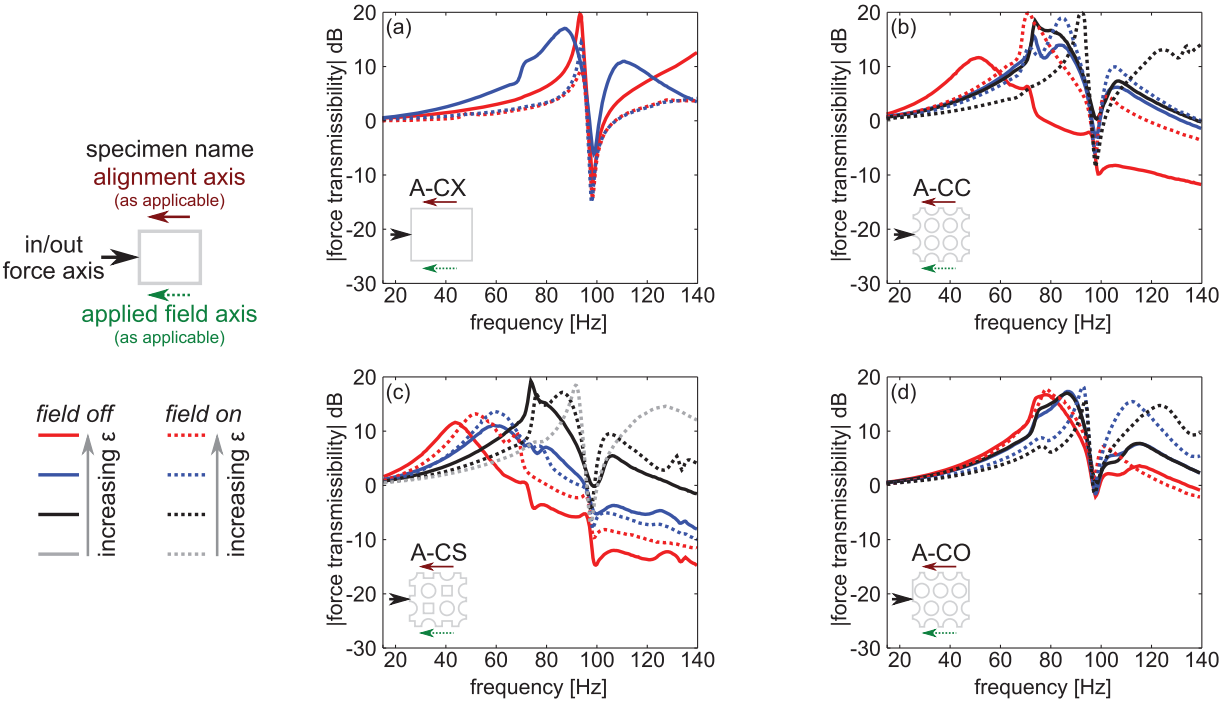

Figure 13. At left are the inset conventions for the specimen class, and excitation, alignment, and field axes, as applicable, and legends for degrees of pre-strain ε shown in the subsequent plots. (a–d) Dynamic force transmissibility measurements for anisotropic (A) specimens excited in axes of particle anisotropy.

Results and discussion

Force transmissibility magnitudes for isotropic specimens are presented in Figure 12. The top left panel of Figure 12 provides a labeling convention and general legend for each sub-figure, to associate the results with the appropriate specimen, loading condition, and applied pre-strain ε value given in Table 3; this labeling convention is also used in Figures 13 and 14. In all

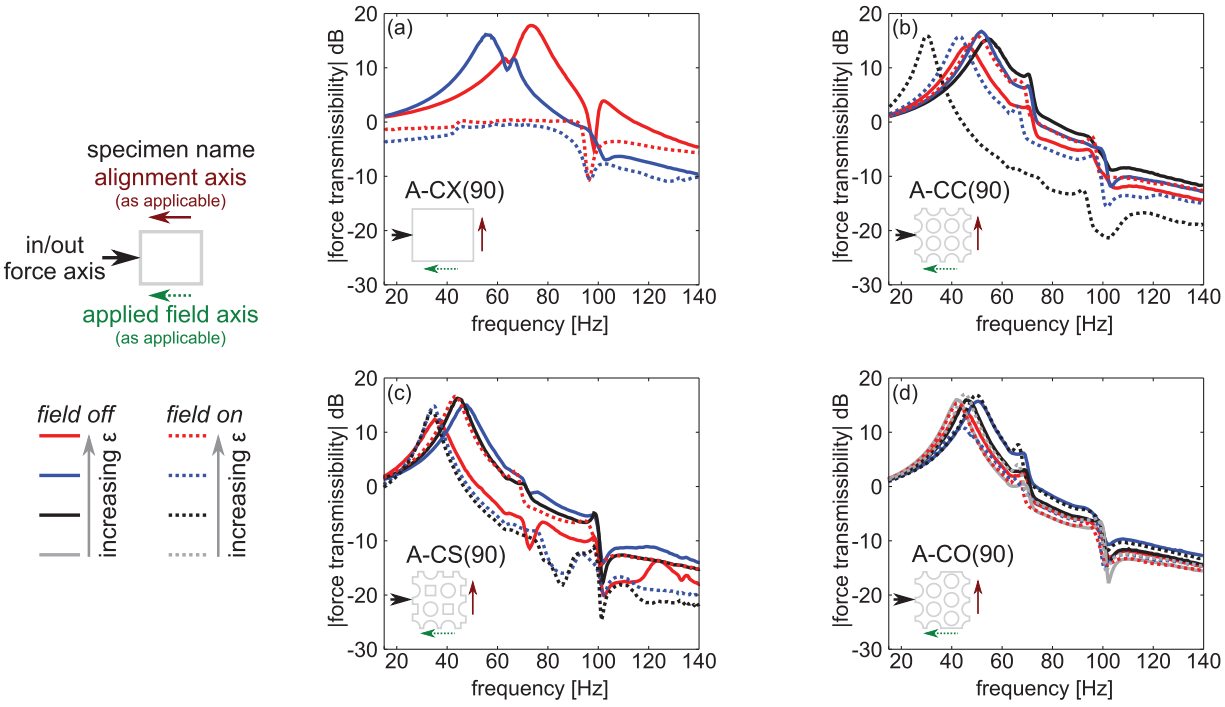

Figure 14. At left are the inset conventions for the specimen class, and excitation, alignment, and field axes, as applicable, and legends for degrees of pre-strain ε shown in the subsequent plots. (a–d) Dynamic force transmissibility measurements for anisotropic (A) specimens excited in axes normal to the axes of particle anisotropy.

force transmissibility measurements acquired and reported here, a narrowband reduction of force transmission occurs around 100 Hz. It is found that this feature is due to the flexibility of the cantilevered MDF excitation plunger. In addition, a feature appears in certain of the measurements presented in Figures 12 to 14 around 70 Hz, although the precise origin of this latter feature near 70 Hz is not conclusively known since it is not uniformly observed. As a result, in Figures 12 to 14, the feature around 100 Hz, specifically spanning about 90 to 110 Hz, should be neglected in consideration of the dynamic force transmissibility measurements for all specimens due to its uniform occurrence and association with a hardware challenge required to acquire data in close proximity to high-strength magnetic fields. Outside of the frequency range of 90–110 Hz, by virtue of the primary mode of response, the remainder of the acquired data is presumed to be unaffected by the excitation plunger resonance, while measurements near to 70 Hz are likewise interpreted with care.

The results of Figure 12 show that application of a magnetic field often results in an increase of the resonant frequency of the specimen, which typically occurs from about 20–80 Hz. Indeed, such behaviors are well known for dynamic properties adaptation of MRE-based systems (Yalcintas and Dai, 2004). A special case where the applied magnetic field reduces the system resonance is observed in Figure 12(d) when a pre-strain is initially applied on the I-CO MM. Indeed, the I-CO MM reveals a notable means of tailoring force transmission at frequencies above the resonance by the magnetic field, Figure 12(d). As suggested by the force transmissibility data, the dramatic and non-uniform collapse evident in Figure 7 may be a source for incoherent force transmission once the magnetic field is applied in order to further contort the internal architecture by rotation of the embedded iron particles. The key underlying processes involved in generating the field-adaptation of force transmission for the I-CO MM are worthy of continued investigation, such as by computational modeling, which is one of our ongoing research focuses.

In contrast with field-driven properties change (Albanese and Cunefare, 2003; Yalcintas and Dai, 2004), the stiffness of MM also changes with respect to pre-strain. According to the experimental results presented in section "Mechanical properties characterization," the magnetic field may control the stiffness of MM via two mechanisms: the formation of iron particle chains and the collapse effect. When the pre-strain is relatively small and thus no collapsing occurs with or without applied magnetic field, the magnetic field in most cases increases the stiffness of MM via forming iron particle chains. When the pre-strain is relatively large and thus collapsing occurs, the magnetic field either increases or reduces the stiffness of MM via tuning the bulk, likely by random contortion of the iron particles within the collapsed MRE material geometries. When the pre-strain is moderate, the stiffness variation of MM due to the applied magnetic field depends on the relative balance and interplay of both

mechanisms. For instance, with the I-CC specimen, Figure 12(b) reveals around 22% and 13% increase in the resonance frequency of the force transmission by activating the magnetic field at low and high pre-strains, respectively. The resonance frequency increment is due to the formation of iron particle chains and the collapse mechanism, respectively. For moderate pre-strain, the applied magnetic field both increases the intrinsic stiffness of MRE via forming iron chains and decreases the stiffness of metamaterials via inducing collapsing. These two mechanisms counteract each other and thus result in less significant resonance adaptation.

Yet, the role of the collapse mechanism for the CS and CO metamaterials is in fact more dramatic than the influence observed for I-CC. Figure 12(c) shows that the collapse nearly reduces by half the peak frequency of force transmission for I-CS while the application of a magnetic field can aid this collapse influence via the additional static compression afforded under such circumstances. For example, for the moderate strain, blue curves in Figure 12(c), the I-CS MM can tailor force transmission by about 15 dB at 48 Hz due to the activation of the magnetic field. No such significant adaptation of dynamic properties is achieved by the pre-strain to the control I-CX specimens, whether or not the magnetic field is applied, Figure 12(a).

It is well known that anisotropic MRE is more responsive to applied magnetic fields than isotropic samples (Dorfmann and Ogden, 2003; Li et al., 2014). This established knowledge is generally exemplified by the evidence of dynamic force transmission adaptation observed in Figures 13 and 14 for anisotropic specimens when compared to corresponding isotropic samples, Figure 12. When the input/output force axis is aligned with the direction of the iron particle alignment of anisotropic specimens, Figure 13 shows that large dynamic stiffness tuning is empowered by activating the magnetic field. For example, the A-CC MM can change the peak frequency of force transmission by about 40% due to application of a field, Figure 13(b), while at frequencies above 60 Hz this corresponds to an adaptation of force transmission of about 10 dB, that is, one order of magnitude change in mechanical power. Comparatively, the A-CS specimen is shown in Figure 13(c) to mutually leverage the bulk collapse mechanism and magnetic field influences to tailor the frequency of peak force transmission by almost 100% (from about 45 to 92 Hz), while 15 dB or greater change in force transmitted through the A-CS may be realized by activating or suppressing the collapse mechanism (via pre-strain ε control) at frequencies above 100 Hz. These examples are greater adaptations of dynamic stiffness properties enabled by the metamaterials when compared to the control A-CX specimen, Figure 13(a). Interestingly, the results of Figure 13(d) appear to suggest that the A-CO specimens provide relatively mild properties change via either the pre-strain (hence, collapse mechanism) or applied field. This is potentially explained by the fact that the specimen is acted upon in the axis that is elastically stiffer by virtue of both the internal void architecture and the particle alignment; as a consequence, the capability for dynamic properties change may be minimized since the applied field can only stiffen the specimen further, which is indeed the finding of the static properties characterization, Figure 10(b) and (d).

When all specimens composed of anisotropic MRE are rotated by 90° with respect to the axes of anisotropic alignment and force application, the adaptation of dynamic properties due to application of a magnetic field is discovered to exhibit a full range of opportunities, according to the selection of the specimen class and pre-strain ε. These results are shown in Figure 14. Not surprisingly, the A-CX(90) specimens are most affected by the field itself, Figure 14(a), since they are composed from the greatest volume of anisotropic MRE and hence respond more severely to the field. Yet, the use of pre-strain on the A-CX(90) specimens only uniformly increases the dynamic stiffness, and the field-induced adaptation does not notably reduce the force transmission below input levels, that is, below 0 dB. In significant contrast, both A-CC(90) and A-CS(90) exhibit a considerable means to reduce force transmission by application of a magnetic field. For instance, Figure 14(b) reveals that for a mild pre-strain ε (black curves), the presence of the magnetic field on A-CC(90) triggers the internal collapse mechanism and thus cuts the peak frequency of force transmission in half (from about 57 to 28 Hz), with the result that the force transmitted at 57 Hz is then reduced by approximately 20 dB, that is, two orders of magnitude in mechanical power. A comparable but less significant change in force transmission is brought on by the application of the magnetic field to the A-CS(90) specimens. In other words, by harnessing the internal topological change (Figure 7) alongside externally applied magnetic fields, the A-CC(90) and A-CS(90) MMs facilitate significant on-demand tuning of dynamic properties, in a similar way the mechanical properties are greatly tuned, see Figures 6(e) and 8(e). In agreement with the findings in Figure 10(c), the dynamic force transmission measurements in Figure 14(d) reveal that the elastic influence of the internal collapse mechanism dominates the adaptation capabilities of the A-CO(90) MMs when compared to the role of the external field. Respectively, considering the vast differences among the specimen measurements in Figure 14 and evidence presented in the prior results, this study conclusively shows that integrating ideas from elastic metamaterials with the established developments in MRE properties modulation cultivates new opportunity via a concept of MMs that may be controlled for real-time adaptations in static and dynamic properties that neither MRE or elastic metamaterials alone offer.

Conclusion

By balancing the influences of pre-strain upon strategic internal void architectures and the magnetic field interactions of material systems composed using MRE materials, this report demonstrates that large mechanical and dynamic properties tuning is able to be leveraged in MMs. Through the experimental studies presented here, several intriguing factors are observed. For instance, internal architectures may be selected so as to induce collapse mechanisms with primary influence upon the properties when compared to the roles of applied magnetic fields, such as the CO(90) MM design. Also, the rotation of certain specimens relative to the applied field may result in "break-away" type influence of the field in governing properties change, such as the A-CC(90) and A-CS(90) specimens that immediately collapse once the field is introduced, even if not pre-strained. The new concept of MMs provides a potential method to modulate MRE material system properties in real-time via balancing the coupled influences of internal void architecture, pre-strain, and applied magnetic fields. The means to fully control these, and other phenomena, for on-demand properties tuning are the focus of our ongoing studies which include numerical modeling to uncover the magnetoelastic coupling at length scales on the order of the internal architectures.

Declaration of Conflicting Interests

The author(s) declared no potential conflicts of interest with respect to the research, authorship, and/or publication of this article.

Funding

The author(s) disclosed receipt of the following financial support for the research, authorship, and/or publication of this article: The authors acknowledge the member organizations of the NSF I/UCRC Smart Vehicle Concepts Center, a National Science Foundation Industry/University Cooperative Research Center created under grant NSF IIP-1238286.

References

Albanese AM and Cunefare KA (2003) Properties of a magnetorheological semi-active vibration absorber. In: *Proceedings of the SPIE 5052: smart structures and materials 2003: damping and isolation*, San Diego, CA, 2 March 2003, pp. 36–43. Bellingham, WA: SPIE.

Bayat A and Gordaninejad F (2015a) Band-gap of a soft magnetorheological phononic crystal. *Journal of Vibration and Acoustics: Transactions of the ASME* 137: 011011.

Bayat A and Gordaninejad F (2015b) Dynamic response of a tunable phononic crystal under applied mechanical and magnetic loadings. *Smart Materials and Structures* 24: 065027.

Bellan C and Bossis G (2002) Field dependence of viscoelastic properties of MR elastomers. *International Journal of Modern Physics B: Condensed Matter Physics, Statistical Physics, Applied Physics* 16: 2447–2453.

Bowen L, Springsteen K, Feldstein H, et al. (2015) Development and validation of a dynamic model of magneto-active elastomer actuation of the origami waterbomb base. *Journal of Mechanisms and Robotics: Transactions of the ASME* 7: 011010.

Chen C and Liao WH (2012) A self-sensing magnetorheological damper with power generation. *Smart Materials and Structures* 21: 025014.

Choi YT and Wereley NM (2009) Self-powered magnetorheological dampers. *Journal of Vibration and Acoustics: Transactions of the ASME* 131: 044501.

Crivaro A, Sheridan R, Frecker M, et al. (2016) Bistable compliant mechanism using magneto active elastomer actuation. *Journal of Intelligent Material Systems and Structures* 27: 2049–2061.

Dorfmann A and Ogden RW (2003) Magnetoelastic modelling of elastomers. *European Journal of Mechanics A: Solids* 22: 497–507.

Lewitzke C and Lee P (2001) Application of elastomeric components for noise and vibration isolation in the automotive industry (SAE international journal of passenger cars—mechanical systems 110). SAE paper 2001-01-1447.

Li Y, Li J, Li W, et al. (2014) A state-of-the-art review on magnetorheological elastomer devices. *Smart Materials and Structures* 23: 123001.

Li Y, Li J, Tian T, et al. (2013) A highly adjustable magnetorheological elastomer base isolator for applications of real-time adaptive control. *Smart Materials and Structures* 22: 095020.

Mayer D, Militzer J and Bein T (2014) Integrated solutions for noise and vibration control in vehicles (SAE international journal of passenger cars—mechanical systems). SAE paper 2014-01-2048.

Mullin T, Deschanel S, Bertoldi K, et al. (2007) Pattern transformation triggered by deformation. *Physical Review Letters* 99: 084301.

Muster D and Plunkett R (1988) Isolation of vibrations. In: Beranek LL (ed.) *Noise and Vibration Control*. Washington, DC: Institute of Noise Control Engineering, pp. 406–433.

Padalka O, Song HJ, Wereley NM, et al. (2010) Stiffness and damping in Fe, Co, and Ni nanowire-based magnetorheological elastomeric composites. *IEEE Transactions on Magnetics* 46: 2275–2277.

Porter L (2007) NASA's new aeronautics research program. In: *Proceedings of the 45th AIAA aerospace sciences meeting and exhibit*, Reno, NV, 8–11 January 2007, pp. 1–49. Reston, VA: AIAA.

Shan S, Kang SH, Wang P, et al. (2014) Harnessing multiple folding mechanisms in soft periodic structures for tunable control of elastic waves. *Advanced Functional Materials* 24: 4935–4942.

Shim J, Shan S, Košmrlj A, et al. (2013) Harnessing instabilities for design of soft reconfigurable auxetic/chiral materials. *Soft Matter* 9: 8198–8202.

Tipton CR, Han E and Mullin T (2012) Magneto-elastic buckling of a soft cellular solid. *Soft Matter* 8: 6880–6883.

Yalcintas M and Dai H (2004) Vibration suppression capabilities of magnetorheological materials based adaptive structures. *Smart Materials and Structures* 13: 1–11.